RSC Advances

ROYAL SOCIETY OF CHEMISTRY

PAPER

View Article Online
View Journal | View Issue

Cite this: *RSC Adv.*, 2024, **14**, 755

A green light emissive $LaSr_2AlO_5:Er^{3+}$ nanocrystalline material for solid state lighting: crystal phase refinement and down-conversion photoluminescence with high thermal stability†

Pawan Kumar,[a] Devender Singh *[a] and Harish Kumar[b]

The present study reveals the structural and optoelectronic characteristics of a down-converted (DC) green luminous Er^{3+} doped $LaSr_2AlO_5$ phosphor that was produced by employing an efficient and reliable gel-combustion process assisted with urea as a fuel. Using Rietveld refinement of diffraction data, the crystal structure and phase formation were examined. The surface morphology and elemental configuration of the phosphor were analyzed *via* TEM and EDX spectroscopy, respectively. The band gap of $LaSr_2AlO_5$ (5.97 eV) and optimized $La_{0.96}Sr_2AlO_5$:4 mol% Er^{3+} (5.51 eV) classify the optimized sample as a direct band-gap material. The PL peaks located in the visible range corresponding to transitions $^2H_{9/2} \rightarrow {}^4I_{15/2}$ (406 nm), $^2H_{11/2} \rightarrow {}^4I_{15/2}$ (520 nm), $^4S_{3/2} \rightarrow {}^4I_{15/2}$ (550 nm), and $^4F_{9/2} \rightarrow {}^4I_{15/2}$ (665 nm) were revealed by photoluminescence spectroscopy under 377 nm excitation. Above 4 mol% Er^{3+} doping, concentration quenching was observed, which was controlled by the quadrupole–quadrupole interaction. Based on the findings of the double exponential fitting of lifetime curves acquired from the emission spectra at λ_{ex} = 377 nm and λ_{em} = 550 nm, the average lifetime of the excited levels of considered nanomaterials was estimated. The temperature-dependent emission spectra of the $La_{0.96}Sr_2AlO_5$:4 mol% Er^{3+} sample were collected in the range 298–498 K. The considered phosphor was found to have a high thermal stability as evidenced by the luminous intensity being sustained at 74.29% at 498 K compared to the intensity at ambient temperature (298 K) with an activation energy of 0.1453 eV. The calculated color purity and superb chromaticity coordinates indicates that the phosphors have a high degree of color purity, which further supports its applicability as a green component in solid-state lighting.

Received 21st October 2023
Accepted 7th December 2023

DOI: 10.1039/d3ra07175h

rsc.li/rsc-advances

1 Introduction

People are becoming more conscious about environmental preservation and energy conservation in the modern world as energy resources become more limited.[1,2] The scientific community is now looking for effective energy-saving gadgets owing to the rising demand for energy in the twenty-first century. In simple terms, phosphors makes LED light usable. LED chips are intrinsically blue, red, or green, with blue LEDs being the most commonly used in solid-state lighting. However, the blue light that they produce is unusable for everyday lighting and must be covered with a phosphor. The phosphor material converts the high-energy light from the LED to a lower-energy (longer wavelength) light. Phosphors can absorb all or a part of the light emitted by the LED. As a result, phosphors produce color wavelengths longer than the absorbed light.[3–5] In light of this, a great deal of work has gone into creating new lighting sources, leading to the introduction of light-emitting diodes (LEDs) and white light-emitting diodes (w-LEDs) as solid-state lighting (SSL) sources.[6–9] Compared to traditional incandescent and halogen lights, LEDs and w-LEDs have the benefits of low energy consumption, durability, extended life, the absence of mercury, and environmental friendliness.[10–12] Due to their benefits, LEDs and w-LEDs have a wide variety of potential applications in the fields of display technology and lighting.

Solid-state lighting was the earliest use of light-emitting diodes after blue light-emitting diodes were developed in the 1990s. In 1997, this innovation led to the creation of white-emitting LEDs by merging a blue-emitting GaN-chip with a yellow phosphor (YAG:Ce).[13,14] Nevertheless, the resultant w-LED has certain shortcomings, including low color temperature stability and a poor color rendering index (CRI).[15,16] The focus of w-LED manufacturing changed from a YAG:Ce phosphor blue LED-based plan to a tri-color (red, green, and blue) phosphor ultraviolet LED-based approach in order to reduce

[a]*Department of Chemistry, Maharshi Dayanand University, Rohtak-124001, Haryana, India. E-mail: devjakhar@gmail.com*

[b]*Department of Chemistry, School of Chemical Sciences, Central University of Haryana, Mahendergarh-123031, India*

† Electronic supplementary information (ESI) available. See DOI: https://doi.org/10.1039/d3ra07175h

these problems.[17,18] In addition to saving a significant amount of energy and lowering environmental pollution, using phosphor-converted w-LEDs instead of conventional lighting equipment is a potent technology with a high color rendering index and adequate color reproduction for efficient lighting.[19,20] The selection of a suitable luminescent host material is considered to be essential in enabling the spectacular uses of RE ions and ensuring their remarkable illuminated properties. Compared to other inorganic materials, aluminates are considered a superior luminous host material for RE ions and have been extensively studied for solid-state lighting purposes.[21,22] $LaSr_2AlO_5$ is an inorganic host substance with *I*4/*mcm* space symmetry with a tetragonal crystal structure.[23] $LaSr_2AlO_5$ has excellent properties, such as a high optical band gap and excellent optical, thermal, and chemical stability.[24] Trivalent erbium (Er^{3+}), one of the lanthanide (Ln^{3+}) ion family, is an efficient down-converting luminescent centre that may be used to create green emissive phosphors by converting NUV light to visible spectrum.[25,26] Moreover, the illuminating characteristics that Er^{3+} ions achieve are highly dependent on the environment of the encompassing host into which these ions are assimilated. For this reason, authors conducted extensive research to find a sustainable host for trivalent erbium ions exhibiting viable properties like superior chemical and thermal durability, reduced toxicity, rigid framework, and high lumen output.[27–29] To modify the optical characteristics of Er^{3+} doped $LaSr_2AlO_5$ luminous nanoparticles and investigate their potential applications in many domains, it is imperative to establish simple synthetic procedures that provide controlled and uniform crystalline phase, shape, and size. This resulted in the development of a number of chemical techniques, such as the microwave-aided method, chemical vapour decomposition, gel-combustion, and sol–gel.[30–33] The gel-combustion technique has been the focus of this study because of its special qualities, which include its simplicity of synthesis, ability to produce high-purity nano-sized crystalline powders at low temperatures, improved homogeneity, and ability to produce high-purity powder.[34–36] In the present study, we discuss the combustion synthesis of $LaSr_2AlO_5$:$x$$Er^{3+}$ (x = 1–7 mol%) phosphors. XRD and SEM/TEM investigations provide structural and morphological information about the synthesized materials. Diffuse reflectance spectra (DRS) and luminescence (PL/PLE) spectra were used to analyze the optical characteristics of the developed nanophosphors. Furthermore, temperature-dependent PL emission spectra of the developed phosphor demonstrated its high thermal stability. The photometric outcomes show that the produced phosphor has good color purity, which suggests that it could be potentially utilized to produce cool green light.

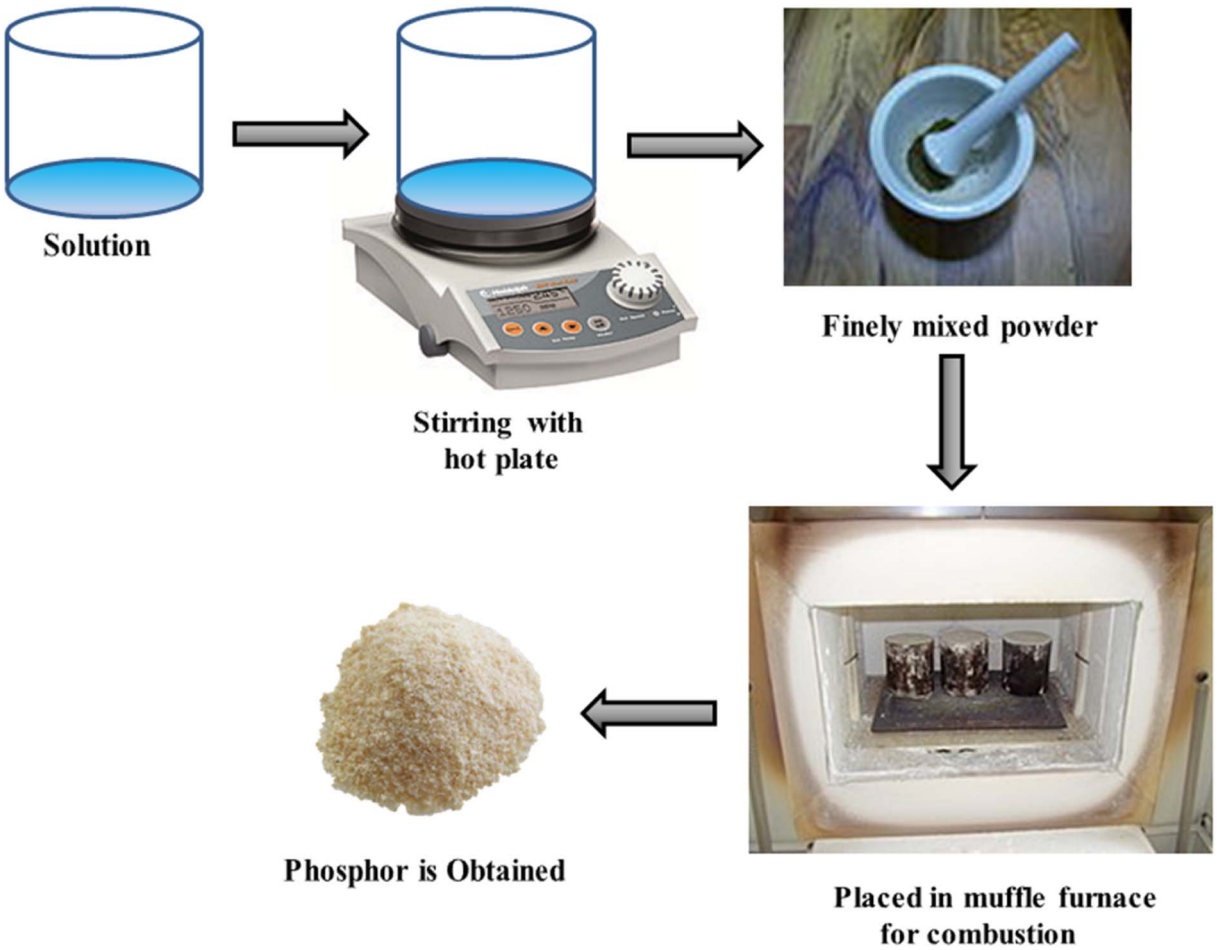

Fig. 1 Schematic diagram of the gel-combustion process used for the synthesis of $LaSr_2AlO_5$:Er^{3+} nanophosphors.

2 Experimental

2.1 Materials and synthesis

A series of green light emissive $La_{(1-x)}Sr_2AlO_5$:x mol% Er^{3+} ($x = 1$–7 mol% Er^{3+}) nanophosphors were produced using a gel-combustion method aided by urea as fuel (Fig. 1). In a beaker, high purity metal nitrates such as $Sr(NO_3)_2$, $La(NO_3)_3 \cdot 6H_2O$, $Er(NO_3)_3 \cdot 6H_2O$, and $Al(NO_3)_2 \cdot 9H_2O$ were mixed in the correct stoichiometric ratio with the calculated amount of urea. The mixture was constantly stirred to achieve a homogeneous solution. The overall oxidizing and reducing valencies in the balanced reaction determine the molar ratio of urea to the metal nitrates. To produce highly uniform oxides with stoichiometric accuracy, urea as fuel is an essential component. Urea serves as a fuel for the redox process after being oxidized by nitrate ions. Energy is delivered by urea in the exothermic method.[37] The beaker was then placed into the preheated furnace and kept at 600 °C for a short time. Dehydration, foaming, and decomposition are the first problems the solution encounters. The required solid appears as a result of the combustible gases generated by this method of igniting and burning with flame.[38] The end product was then removed from the furnace, permitted to cool at normal temperature, and thoroughly crushed into powder. The obtained powder materials underwent further calcination to achieve the desired phase.

2.2 Instrumentations

The X-ray diffraction patterns of produced samples were recorded on a Rigaku Ultima-IV diffractometer, which scans at a rate of 2° min^{-1}. This allowed for the examination of phase purity and crystallinity of the samples. Cu-Kα was utilized as the radiation. Also, 40 kV and 40 mA were maintained as the constant tube voltage and current, respectively. Match! 3.0 Rietveld refinement software was used for the refining process to analyze materials in both qualitative and quantitative aspects. TECNAI transmission electron microscope (200 kV) was used to analyze the morphology and particle size. Ametek energy dispersive X-ray spectrometer was used for elemental analysis to determine the chemical composition of the synthesized phosphors. A Horiba Jobin YVON Fluorolog spectrophotometer aided by xenon light was used to analyze the excitation and emission spectra of the materials at room temperature.

3 Results and discussion

3.1 XRD evaluation

The phase purity, crystal structure, and crystallinity of the undoped $LaSr_2AlO_5$ and Er^{3+} (1–7 mol%) doped $LaSr_2AlO_5$ nanomaterials were assessed *via* X-ray diffraction. The XRD patterns of undoped and different (1–7 mol%) Er^{3+} doped $LaSr_2AlO_5$ nanophosphors are displayed in Fig. 2(a), which were captured at room temperature within a 2θ scanning range of 10°–80°. The standard reference used in this case was the diffraction data of $EuSr_2AlO_5$ nanomaterial shown in Fig. 2(a), representing JCPDS No. 70-2197.[39] The experimental diffraction data and reference data are in good accordance with each other with respect to their location and relative intensity of diffraction lines, which further affirm the phase excellence and monophasic nature of the synthesized nanomaterials. The tetragonal class (reference material) with *I*4/*mcm* space (140) group symmetry was perceived in undoped $LaSr_2AlO_5$ and all samples

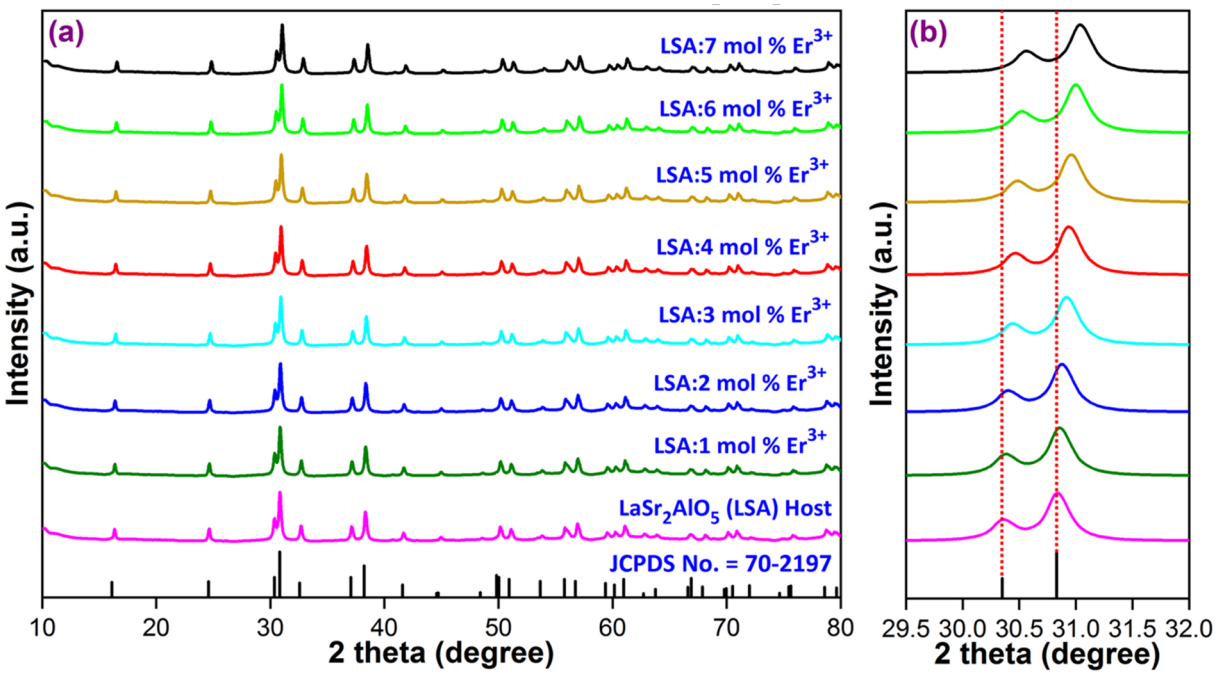

Fig. 2 (a) Diffraction patterns of $LaSr_2AlO_5$ and $La_{1-x}Sr_2AlO_5$:xEr^{3+} ($x = 1$–7 mol%) phosphors; (b) an enlarged pattern view of all considered samples.

Table 1 The interplanar d-spacing values of the host and Er^{3+} (1–7 mol%) doped phosphors

Sample	2θ angle	d-Spacing (Å)
$LaSr_2AlO_5$ (LSA)	30.82	2.8989
LSA:1 mol% Er^{3+}	30.85	2.8961
LSA:2 mol% Er^{3+}	30.87	2.8943
LSA:3 mol% Er^{3+}	30.90	2.8915
LSA:4 mol% Er^{3+}	30.94	2.8879
LSA:5 mol% Er^{3+}	30.96	2.8861
LSA:6 mol% Er^{3+}	30.99	2.8834
LSA:7 mol% Er^{3+}	31.03	2.8797

of $LaSr_2AlO_5$ doped with Er^{3+} (1–7 mol%) phosphors. The crystal structure of the synthesized material remains the same at different doping levels of Er^{3+} ions. Nonetheless, peaks in the doped samples were found to vary in position, indicating that the dopant Er^{3+} ion was properly incorporated into the $LaSr_2AlO_5$ lattice. Fig. 2(b) demonstrates the enlarged view of the diffraction patterns of the host as well as all doped samples. It is clear from Fig. 2(b) that the diffraction peaks of doped samples moved towards the greater 2θ angle due to the incorporation of the smaller Er^{3+} ions. Additionally, the interplanar spacing (d) values associated with the sharpest peak (202) were calculated and found to decrease in a predictable manner with increasing Er^{3+} ion doping levels (Table 1). These outcomes were caused by the smaller activated cation replacing the larger host cation. Hence, these results were further validated by the Bragg's hypothesis ($2d \sin\theta = n\lambda$).[40] The effective ionic radii for La^{3+} and Er^{3+} ions in the $LaSr_2AlO_5$ matrix are 1.16 Å (CN = 8) and 1.004 Å (CN = 8), respectively. It is believed that Er^{3+} ions occupied the positions of La^{3+} ions in the crystal structure. The difference in ionic radius between the activator and host ions is allowed to be up to 30%. The radii% variance (D_r) between active (Er^{3+}) ions and likely substituted La^{3+} in the $LaSr_2AlO_5$ matrix was deliberated using the following formula (1).[41]

$$D_r = \frac{R_h(CN) - R_d(CN)}{R_h(CN)} \times 100\% \quad (1)$$

Thus, it can be shown that the activator ions successfully replaced the host ions in the present investigation since the computed difference between the activator and host cations is 13.44%. The Debye–Scherrer approach uses the peak broadening analysis to assess the crystallite size. This method uses eqn (2) to calculate the average crystallite size.[42]

$$D_{hkl} = \frac{k\lambda}{\beta(2\theta)\cos\theta} \quad (2)$$

Here, λ denotes the used X-ray wavelength, β defines the FWHM value of the peak, 2θ is the scattering Bragg angle, and k is a constant (0.89). The average particle size data can potentially be exploited to calculate the dislocation density of the host and different doped samples. The number of dislocation lines per unit volume of the crystal is represented by the dislocation density value, which serves as a metric for the size of crystal defects. Additionally, the dislocation density will indicate the degree of crystallinity present in the nanoparticle. Eqn (3) may be used to compute the dislocation density.[43]

$$\text{Dislocation density} = \frac{1}{D^2} \quad (3)$$

Table 2 provides the dislocation density and crystallite size as a function of dopant ion concentration. The calculation demonstrates that the nanoparticles produced in this work have a rather low dislocation density. A low dislocation density indicates a high degree of crystallinity in the synthesized nanoparticles.

3.1.1 Williamson–Hall (W–H) analysis. For the W–H plot, strain broadening and size widening must be combined. The W–H technique is the most convenient integral breadth method for distinguishing between the strain-dependent line broadening and crystallite size by analyzing peak width as a function of 2-theta. To show how the lattice strain causes peak broadening, one can utilize the Stokes–Wilson formula (4).

$$\beta_{strain} = 4\varepsilon \tan\theta \quad (4)$$

Consequently, the overall broadening caused by the size and strain in a specific peak with hkl-value may be given as;

$$\beta_{hkl} = \beta_{size} + \beta_{strain} \quad (5)$$

Here, β_{hkl} is used for the FWHM of the various XRD lines.

$$\beta_{hkl} = \frac{K\lambda}{D\cos\theta} + 4\varepsilon \tan\theta \quad (6)$$

Table 2 Computed diffraction values of $LaSr_2AlO_5$ and $La_{1-x}Sr_2AlO_5$:xEr^{3+} (x = 1–7 mol%) nanophosphors

Sample (LSA)	2 theta (2θ)	FWHM	Crystallite size (nm)		Dislocation density (10^{-4})	Microstrain ($\varepsilon \times 10^{-4}$)
			Scherrer's	W–H		
$LaSr_2AlO_5$ (LSA)	30.82	0.2173	39.61	45.17	6.37	4.7425
LSA:1 mol% Er^{3+}	30.85	0.2204	39.05	43.12	6.56	5.2127
LSA:2 mol% Er^{3+}	30.87	0.2221	38.76	42.54	6.66	5.8204
LSA:3 mol% Er^{3+}	30.90	0.2241	38.41	41.10	6.78	6.2487
LSA:4 mol% Er^{3+}	30.94	0.2298	37.46	39.78	7.12	6.3687
LSA:5 mol% Er^{3+}	30.96	0.2331	36.94	38.11	7.33	7.2671
LSA:6 mol% Er^{3+}	30.99	0.2403	35.83	36.81	7.79	8.0457
LSA:7 mol% Er^{3+}	31.03	0.2538	33.93	35.72	8.69	9.2486

On modifying the above eqn (6), we obtained[44,45]

$$\beta_{hkl} \cos \theta_{hkl} = \frac{K\lambda}{D} + 4\varepsilon \sin \theta_{hkl} \quad (7)$$

Eqn (7) takes into account the isotropic nature of the crystal, *i.e.*, all parameters are independent of the direction along which they are evaluated. Hence, the microstrain was taken to be the same in all crystallographic orientations. Plotting the term $\beta \cos \theta$ *vs.* $4 \sin \theta$ for the tetragonal phase favored the alignment of peaks in the samples under consideration (Fig. 3). In the linear fitted plot, the slope and intersect indicate strain and particle size, respectively. All the obtained values corresponding to the microstrain and crystallite size for focused materials are summarized in Table 2.

3.1.2 Rietveld refinement and crystal structure. Employing the Rietveld refinement technique, a typical crystal shape of the synthesized material was developed in order to identify the occupancy of rare earth (Er^{3+}) ions in the $LaSr_2AlO_5$ lattice. Refinement results corresponding to the host (LSA) material and the optimized (LSA:4 mol% Er^{3+}) sample are displayed in Fig. 4(a) and (b), and it is very clear from the fitting profiles that the calculated results are in good agreement with the experimental values. The refinement outcomes show the synthesized samples having a tetragonal system with the *I*4/*mcm* space group. The superiority of the Rietveld refinement is demonstrated through the residuals R_p, R_{wp} and simplified χ^2. These goodness factors are defined by various eqn (S1)–(S4).†[46] In these equations, I_0, I_c and w stand for measured and calculated peak intensities and weighting factor, respectively. Also, N_{obs} and N_{var} define the data points and fitting characteristics, respectively. From the refinement outcomes, R_p and R_{wp} factors were 5.10%, 5.52% and 7.59%, 9.58% and the reduced chi-square value (χ^2) = 2.17 and 2.31 for the host and optimized sample, respectively, showing good convergence of fit. All the refinement data corresponding to the host and optimized sample are summarized in Table 3. According to the results summarized in Table 3, the doped optimized sample's values for unit cell parameters (*a*, *b*, and *c*) were found to be lower than those of the host sample. This was likely caused by the smaller dopant ions replacing the larger host ions. Additionally, the doped sample's unit cell volume seems to have reduced. These results collectively demonstrate that the host material was successfully doped with Er^{3+} ions.

Fig. 5 illustrates the $LaSr_2AlO_5$ crystal structure and provides information about the luminous centre of the host and the doping of activator ions. [La/SrO_8], [SrO_{10}], and [AlO_4] units comprise the three kinds of polyhedra that together make up the $LaSr_2AlO_5$ crystalline structure.[47] Host La^{3+} ions are located at half of 8h crystallographic sites in this structure, forming an

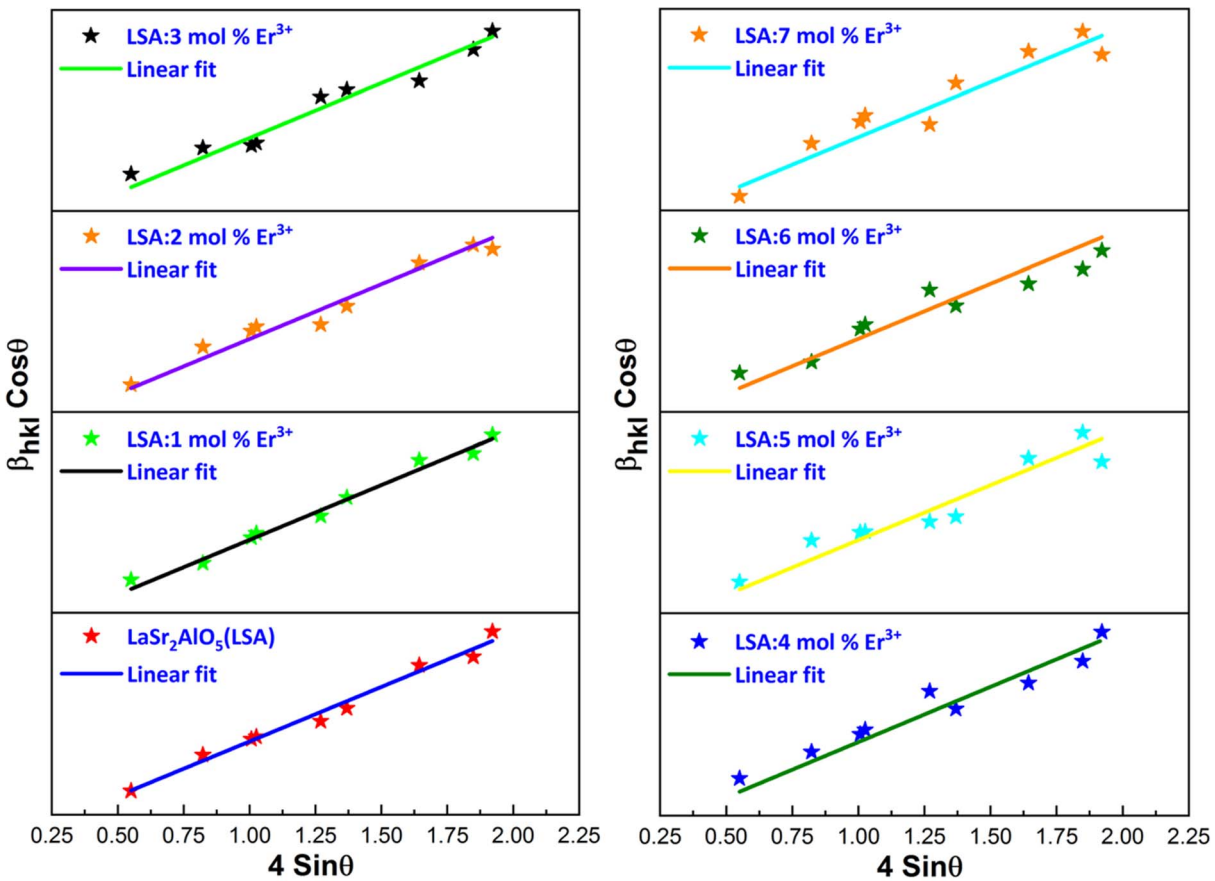

Fig. 3 W–H plot for the host and different doped $La_{1-x}Sr_2AlO_5$:xEr^{3+} (x = 1–7 mol%) samples.

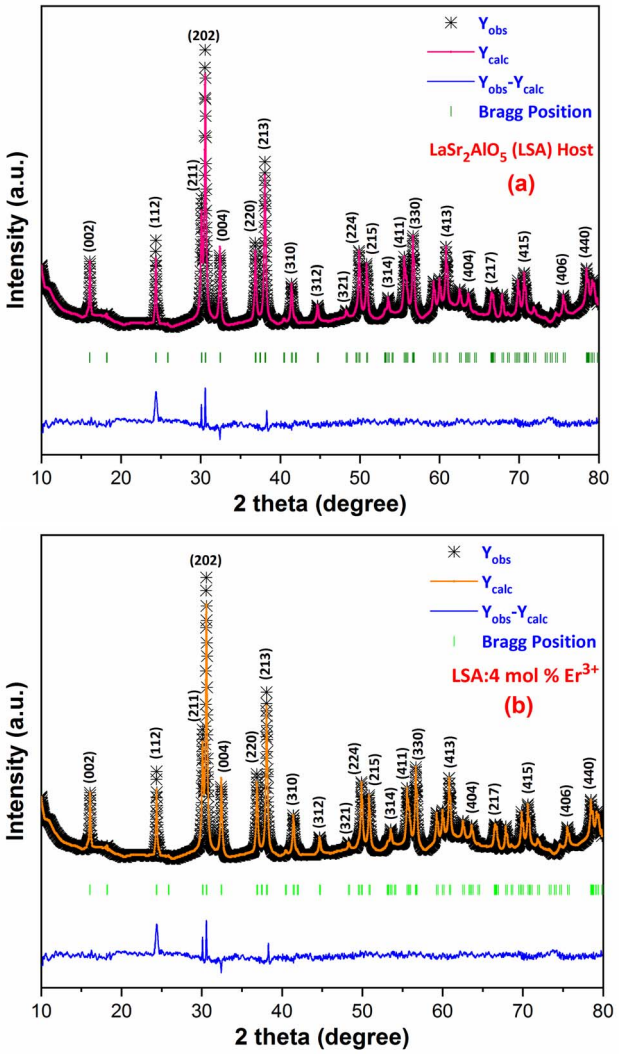

Fig. 4 Rietveld profiles of (a) undoped $LaSr_2AlO_5$ and (b) $La_{0.96}Sr_2AlO_5$:4 mol% Er^{3+} samples.

Table 3 Rietveld refinement parameters of $LaSr_2AlO_5$ and optimal $La_{0.96}Sr_2AlO_5$:4 mol% Er^{3+} nanophosphors

Sample	$LaSr_2AlO_5$	LSA:4 mol% Er^{3+}
Formula weight	421.09	422.21
System	Tetragonal	Tetragonal
2θ range; step (deg.)	10–80; 0.02	10–80; 0.02
Wavelength (Å)	1.54056	1.54056
Space group	*I*4/*mcm*	*I*4/*mcm*
Space group number	140	140
Pearson symbol	tI	tI
Formula unit	4	4
Lattice-symbol	I	I
a (Å)	6.7884	6.7135
b (Å)	6.7684	6.7135
c (Å)	10.9341	10.8209
Volume (Å^3)	503.869	487.70
$\alpha = \beta = \gamma$	90.00	90.00
χ^2	2.17	2.31
R_p (%)	5.10	5.52
R_{wp} (%)	7.59	9.58

eight-fold coordination polyhedral unit called [La(1)O_8]. Also, Sr^{2+} has two distinct sites, *i.e.*, Sr(2) occupies the other half of the 8h atomic locations and forms the [Sr(2)O_8] polyhedral, whereas Sr(3) occupies the 4a positions and forms [Sr(3)O_{10}] coordinated polyhedra. Al(4)O_4 unit is a coordination of four oxygen atoms with Al in the 4b crystal locations. The remaining 4c and 16l sites are occupied by O(5) and O(6), respectively. Table S1† provides a summary of the occupancy factors, atomic coordinates, sites, and isotropic displacement parameters obtained for the $LaSr_2AlO_5$ sample.

3.2 TEM analysis

Utilizing TEM images of the $LaSr_2AlO_5$:Er^{3+} phosphor, the structure, framework, and crystal size of samples were analyzed. Fig. 6 displays the TEM micrograph of the optimized sample. The homogeneously dispersed particles on the surface are approximately spherical in shape and vary in size from 32 to 45 nm. The uneven distribution of heat and mass flow during combustion caused small discrepancies in crystallite size.[48,49] The crystal size obtained from the TEM examination correlates well with the XRD measurements.

3.3 EDX investigation

EDX is a frequently used technique to determine the elemental composition in a small region of the sample. Higher energy electrons from the outer shell inhabit the holes left by the expelled electrons from an electron bombardment in the inner shell of the atom. Identical X-rays with specific energy emanate as electrons migrate from the outer to the inner shell. The measurement of the amount and wavelength of X-rays generated allows for the confirmation of the identification of specific components in the material under examination. Fig. 7(a) and (b) reveal the EDX profiles of undoped $LaSr_2AlO_5$ and Er^{3+} (4 mol%) doped $LaSr_2AlO_5$, respectively. In addition to small peaks from dopant Er^{3+} ions in the doped $LaSr_2AlO_5$ phosphor, the profile shows large peaks for the La, Sr, Al, and O elements. It shows how well the Er^{3+} ions are incorporated into the host matrix. Inset of Fig. 7(a) and (b) shows data in the form of a table compiling the findings of the quantitative EDX study performed on the undoped and Er^{3+} doped samples.

3.4 Photoluminescence study

3.4.1 Excitation and emission spectra. In order to examine the luminous characteristics of nanomaterials, the PLE spectrum at a fixed characteristic PL wavelength of ~548 nm of Er^{3+} has been recorded within the wavelength region of 200–540 nm. The PLE profile of LSA:4 mol% Er^{3+} is illustrated in Fig. 8. The charge transfer band for $O^{2-} \rightarrow Er^{3+}$ is signified by a broad band from 220 to 280 nm with numerous excitation peaks at ~351 nm, ~363 nm, ~377 nm, ~407 nm, ~448 nm, ~488 nm, and ~521 nm.[50] The most significant signal detected at ~377 nm is associated with the $^4I_{15/2} \rightarrow {}^4G_{11/2}$ transition of Er^{3+} ions, revealing that the present phosphor may be advantageous in developing NUV-based LEDs. In addition, peaks are observed at 351 nm ($^4I_{15/2} \rightarrow {}^4G_{7/2}$), 363 nm ($^4I_{15/2} \rightarrow {}^4G_{9/2}$), 407 nm ($^4I_{15/2} \rightarrow {}^2H_{9/2}$), 448 nm ($^4I_{15/2} \rightarrow {}^4F_{5/2}$), 488 nm ($^4I_{15/2} \rightarrow {}^4F_{7/2}$), and

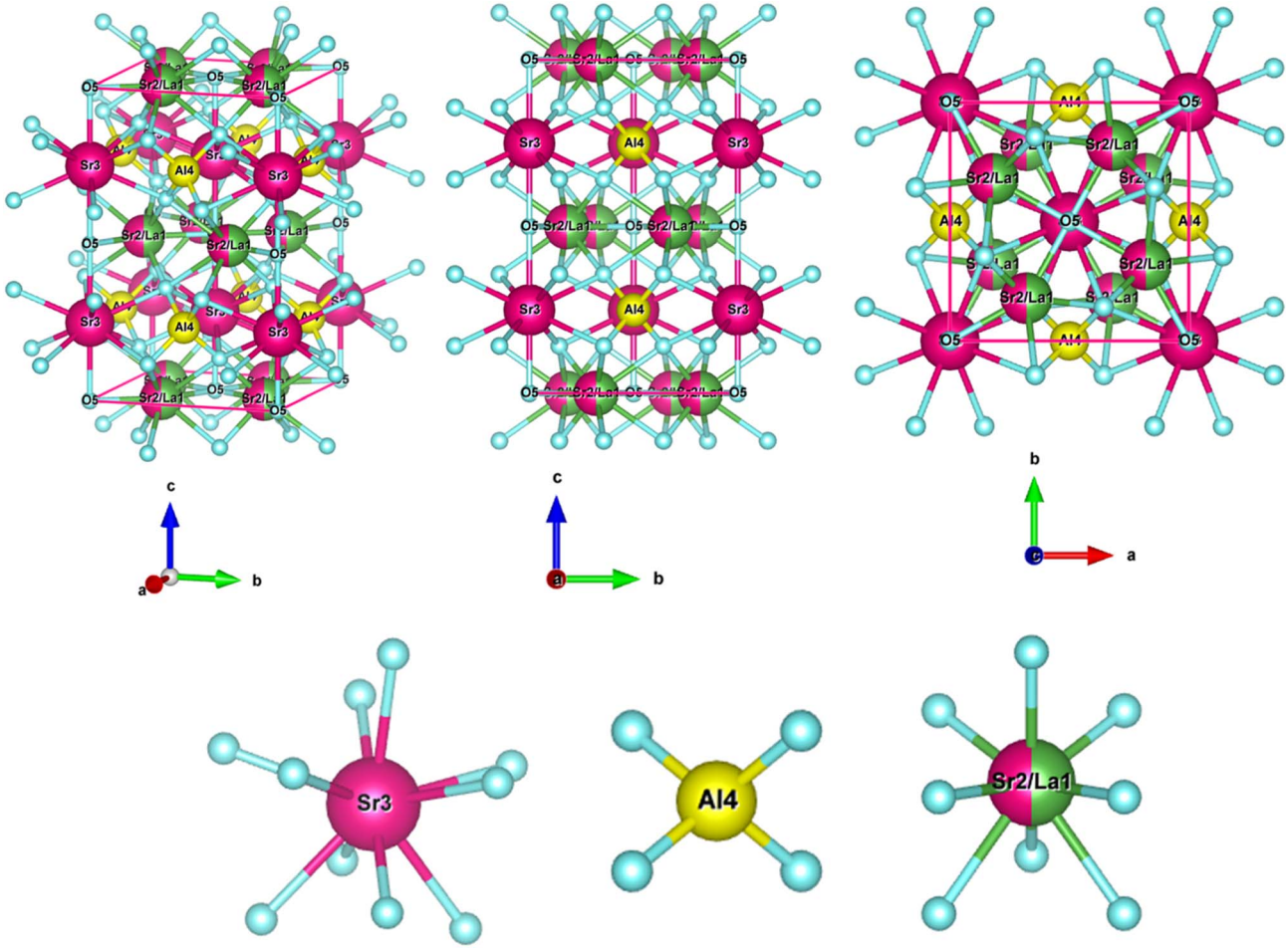

Fig. 5 Crystal structure of $LaSr_2AlO_5$ along with the coordinative environment of various cations.

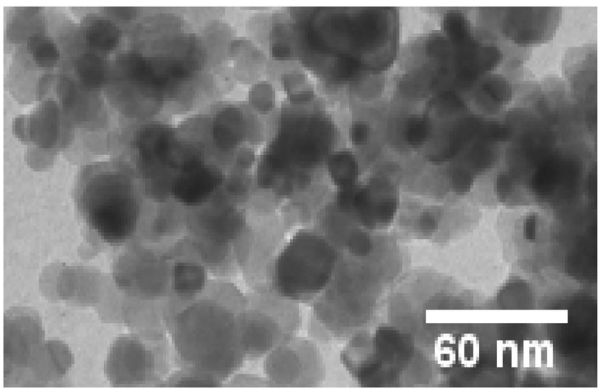

Fig. 6 TEM micrograph of the $La_{0.96}Sr_2AlO_5$:4 mol% Er^{3+} nanophosphor.

521 nm ($^4I_{15/2} \rightarrow {}^2H_{11/2}$).[51] Photoluminescence emission spectra have been obtained at an excitation wavelength of 377 nm, as displayed in Fig. 9. The PL profile demonstrates various emissive peaks centered at ~406 nm with blue emission having $^2H_{9/2} \rightarrow {}^4I_{15/2}$ transition, ~520 nm with green emission having transition $^2H_{11/2} \rightarrow {}^4I_{15/2}$, ~550 nm with strong green emission from $^4S_{3/2} \rightarrow {}^4I_{15/2}$ transition, and red emissive peak at ~665 nm with $^4F_{9/2} \rightarrow {}^4I_{15/2}$ transition.[52] The prominent peak at ~550 nm is caused by the $^4S_{3/2} \rightarrow {}^4I_{15/2}$ transition, which has a value $\Delta J = 6$, indicating that it is an electric dipole (ED) transition and responsible for the green emission observed in synthesized nanophosphors. Various transition states corresponding to the Er^{3+} ion in focused nanophosphors are represented in Fig. 10.

3.4.2 Concentration quenching. The peak intensities increased as the Er^{3+} content increased to 4 mol% of Er^{3+} ions, as shown in Fig. 11. After that point, the emission peak intensities were observed to decline. Concentration quenching (CQ) is the main cause of the emission intensities reducing after the optimal Er^{3+} concentration. Non-radiative energy transfer is primarily responsible for the luminance quenching in the phosphor material within the same rare earth ions. It is commonly known that the spacing between the doping ions is reduced when the amount of doping is consistently raised. In order to calculate the critical distance (R_c) between the rare earth ions, eqn (8) was proposed by Blasse, which is given below.[53]

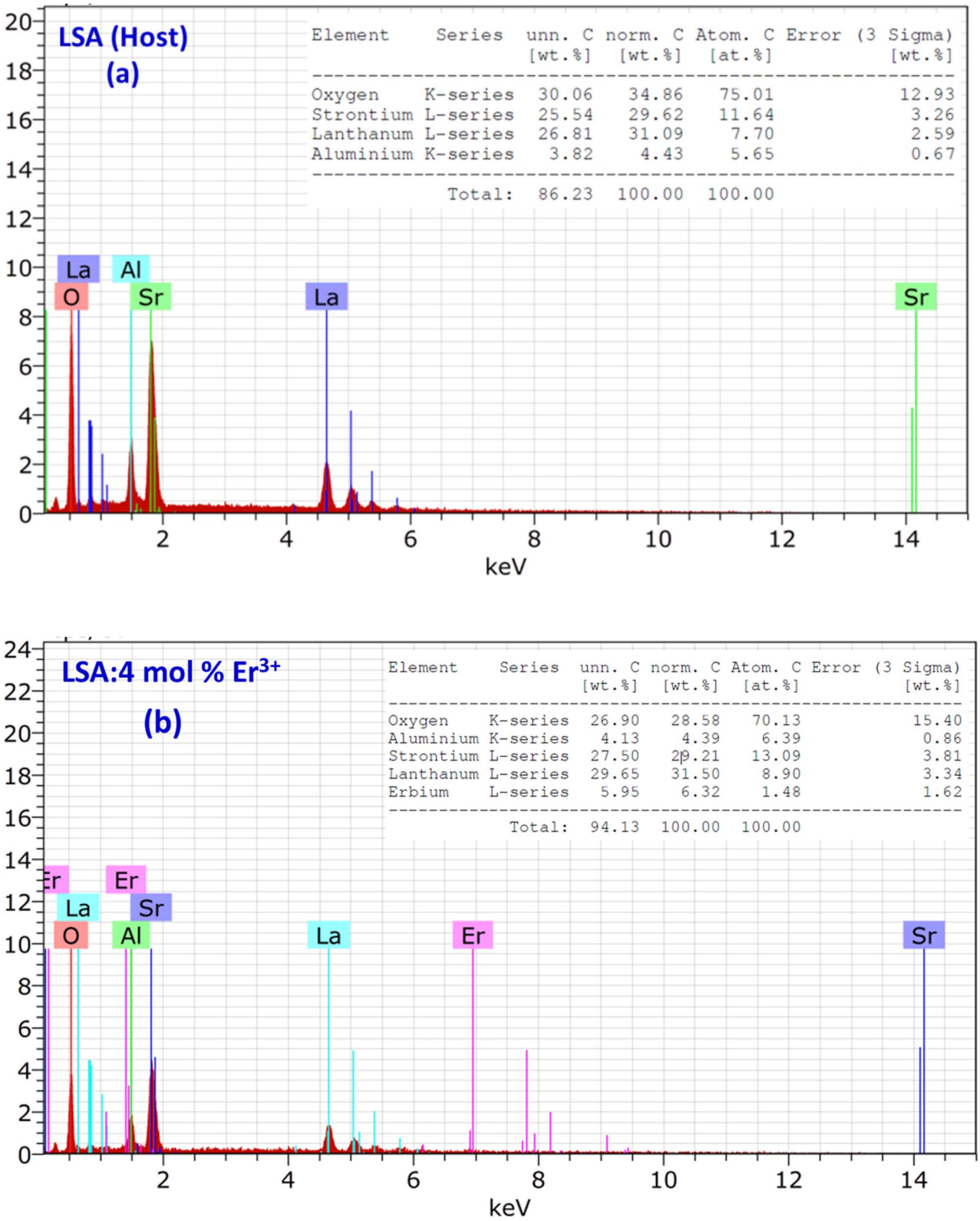

Fig. 7 EDX profiles of the (a) $LaSr_2AlO_5$ (b) $La_{0.96}Sr_2AlO_5$:4 mol% Er^{3+} nanophosphor and the inset represents the atomic and weight percentages of the respective samples.

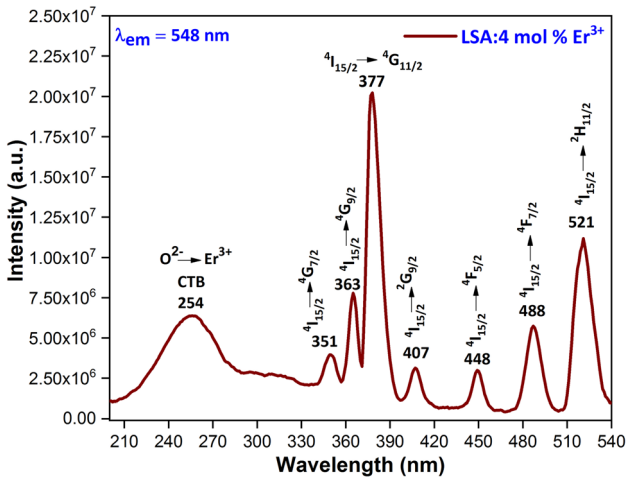

Fig. 8 Excitation spectrum of the $La_{0.96}Sr_2AlO_5$:4 mol% Er^{3+} nanophosphor.

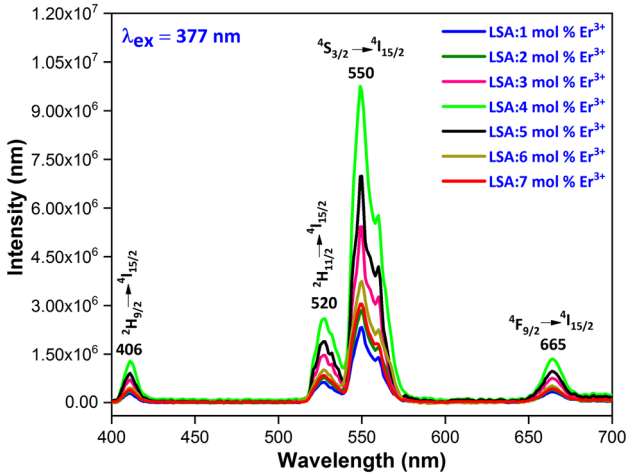

Fig. 9 Emission spectra of the $La_{1-x}Sr_2AlO_5$:xEr^{3+} (x = 1–7 mol% Er^{3+}) nanophosphors.

$$R_c = 2\left(\frac{3V}{4\pi x_c N}\right)^{1/3} \quad (8)$$

Here, x_c, V, and N denote the critical amount of activator ion, volume of unit cell, and number of existing locations per unit cell, respectively. For LSA phosphors doped with Er^{3+}, these values are x_c = 4 mol%, V = 487.70.107 Å, and N = 4. The R_c value was therefore determined to be 17.88 Å. The Blasse theory states that reabsorption, exchange interaction, and multipolar interaction are the three possible non-radiative energy transmission mechanisms between rare earth ions. Radiative reabsorption takes precedence when there is a significant overlap between excitation and emission. CQ occurs due to the exchange interaction when R_c is smaller than 5 Å. Concentration quenching occurs due to the multipolar interaction when the critical distance exceeds 5 Å. Since the observed R_c value in this work is more than 5 Å, concentration quenching is primarily driven by the multipole–multipole interaction. Three types of interactions are included in the multipole–multipole interaction: dipole–dipole (d–d), dipole–quadrupole (d–q), and quadrupole–quadrupole (q–q). The following formula (9) provides the PL emission intensity (I) for each activator amount (x) in accordance with the Dexter theory.[54]

$$\log\left(\frac{I}{x}\right) = k - \frac{Q}{3}\log(x) \quad (9)$$

The plot of $\log(I/x)$ *vs.* $\log(x)$ is fitted linearly using the luminescence intensity of Er^{3+} concentration in the LSA host matrix, as shown in Fig. 12. Fitting eqn (9) yielded a slope of −3.28. The value of Q is calculated as 9.84, which is close to 10. This result validates that the quadrupole–quadrupole interaction was responsible for concentration quenching in Er^{3+} activated $LaSr_2AlO_5$ nanophosphors.

3.5 Luminescence lifetime

When a phosphor radiatively decays from an excited level to the ground state, light is released. The dynamics of illumination, quenching, and energy transfer mechanism are all explained by the decay lifetime. For the purpose of recording the luminescence lifetime data, the excitation and emission wavelengths were fixed at 377 nm and 550 nm, respectively. The recorded decay curve for the optimum (4 mol%) concentration of LSA:Er^{3+} phosphor is depicted in Fig. 13. Numerous exponential functions were employed to precisely match the acquired data. The double exponential function listed below yields the best outcome.[55]

$$I_t = I_0 + A_1\exp(-t/\tau_1) + A_2\exp(-t/\tau_2) \quad (10)$$

Here, I is the luminous intensity, t is the time, A_1 and A_2 are fitting parameters, and τ_1 and τ_2 are the slow and fast components. The average lifetime may also be estimated by putting the values of A_1, A_2, τ_1 and τ_2 into the following eqn (11).

$$\tau_{avg} = (A_1t_1^2 + A_2t_2^2)/(A_1t_1 + A_2t_2) \quad (11)$$

According to the fitting results, when x = 1, 2, 3, 4, 5, 6, and 7 mol% of Er^{3+}, the average decay times of $La_{(1-x)}Er_xSr_2AlO_5$ nanophosphors are 1.431, 1.344, 1.227, 1.134, 1.059, 0.978, and 0.703, respectively. As a result of the non-radiative energy transfer, the average lifespan rapidly declines as the concentration of Er^{3+} rises. Additionally, the radiative lifetime was assessed using Auzel's model to analyze the variance in luminescence lifespan with increasing dopant concentration.

$$\tau_c = \tau_0/1 + \frac{C}{C_0}e^{-N/3} \quad (12)$$

In the above relation, τ_c, c_o, τ_o and N represent the lifetime at concentration c, concentration constant, intrinsic radiative lifetime, and number of phonons, respectively. Quantum efficiency (η) describes the converting ability of the system between

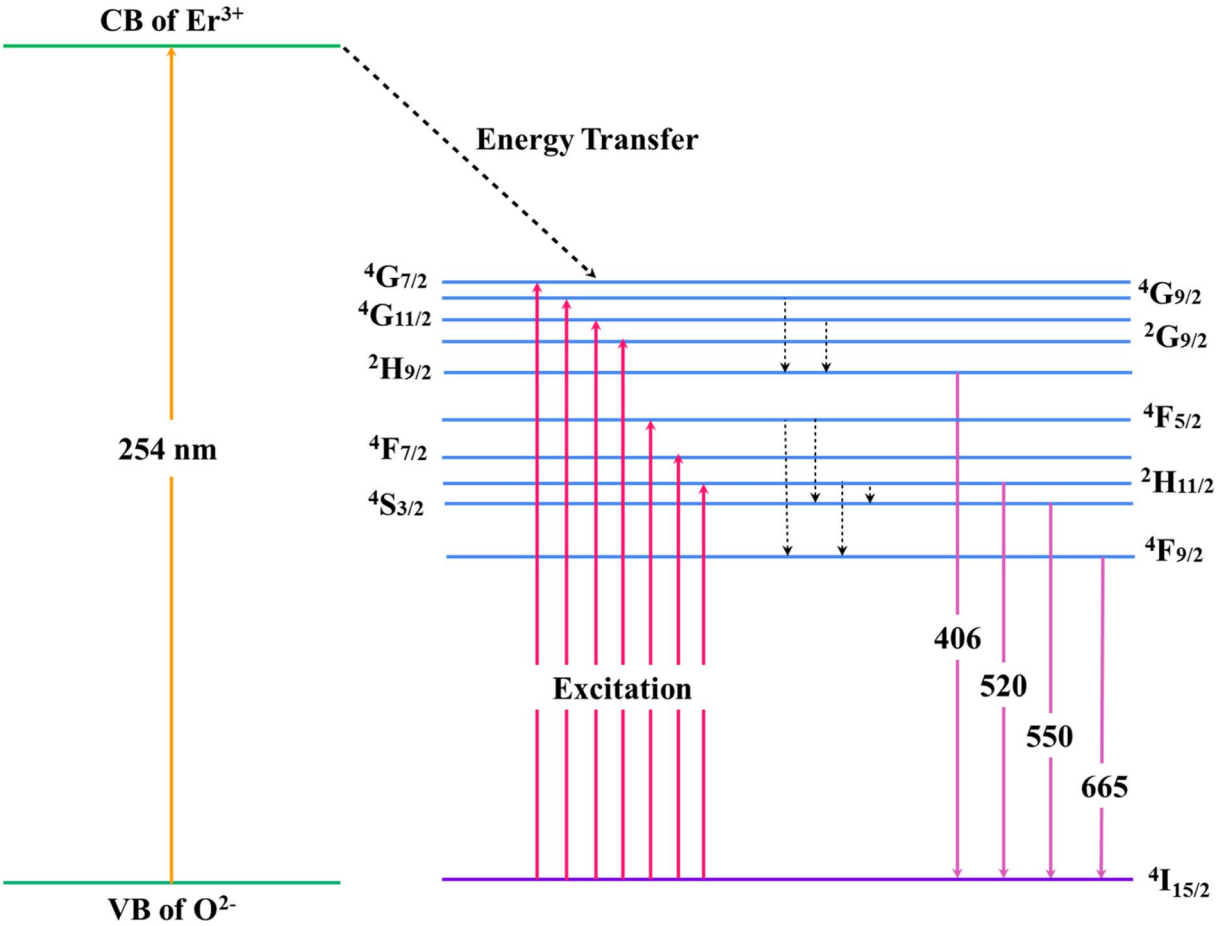

Fig. 10 Pictorial representation of different energy states of Er^{3+} ion in the considered nanophosphors.

input and output. Quantum efficiency of a 4f emitting level depends on the radiative (A_R) and non-radiative (A_{NR}) rates due to deactivation processes of the emitting level. The computed value of $^4S_{3/2}$ emitting states $\tau_o = 1.681$ ms, obtained from the fitting procedure (inset of Fig. 13), was valuable for deriving the quantum efficiency employing the subsequent eqn (13).[56]

$$\eta = \frac{A_R}{A_R + A_{NR}} = \frac{\tau_{avg}}{\tau_0} \quad (13)$$

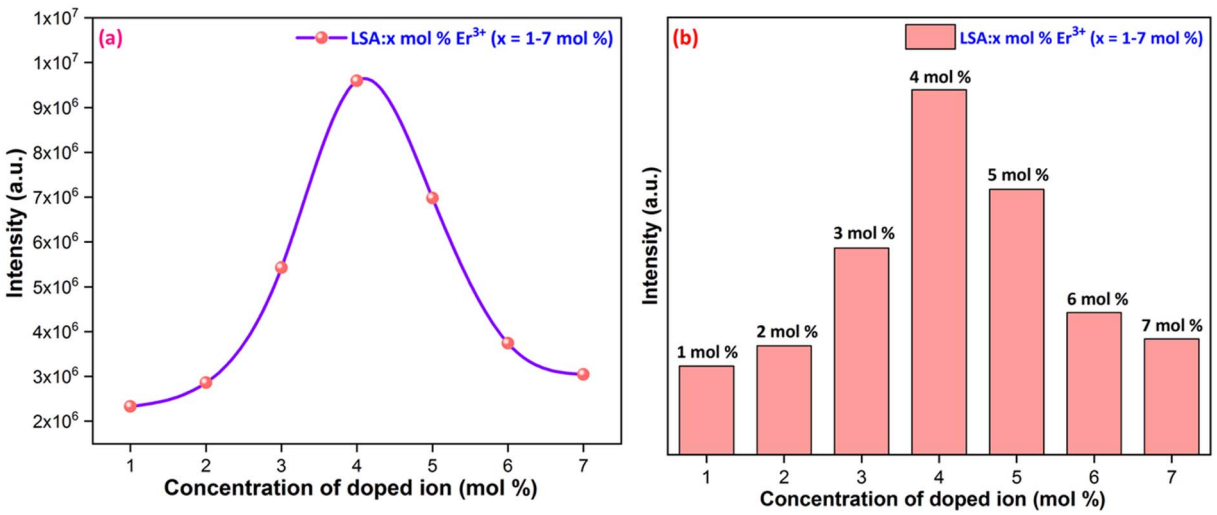

Fig. 11 Concentration quenching profiles of the considered nanophosphors.

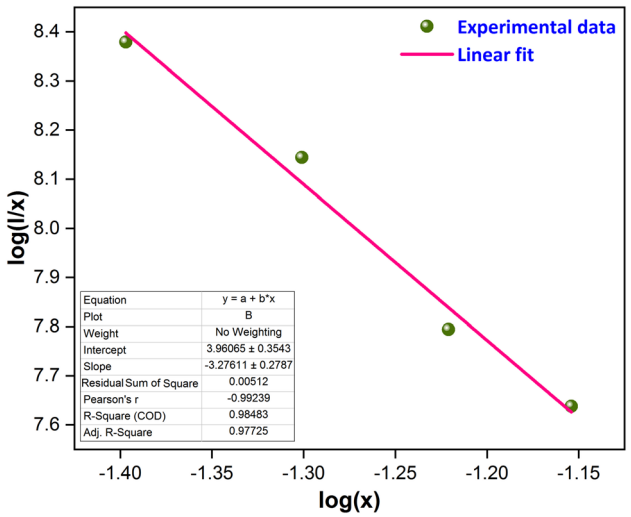

Fig. 12 Straight line fitted graph between log(*x*) and log(*I*/*x*).

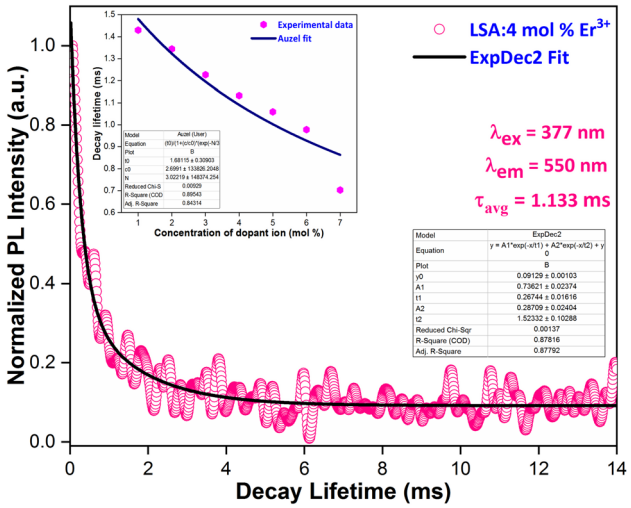

Fig. 13 Decay lifetime profile of the $La_{0.96}Sr_2AlO_5$:4 mol% Er^{3+} nanophosphor and the inset represents the Auzel fitted graph for all doped samples.

Employing the radiative lifetime (τ_o), observed lifetime (τ_{avg}), and the following relationship, the total non-radiative relaxation rates (A_{NR}) are also computed.

$$\frac{1}{\tau_{avg}} = \frac{1}{\tau_0} + A_{NR} \tag{14}$$

Table 4 lists the non-radiative transition rate and quantum efficiency values of the synthesized nanophosphors. It was feasible to effectively integrate the nanomaterials into white light-emitting diodes for illumination because their synthesis produced incredibly high quantum efficiency values.

3.6 Optical absorption analysis

In the realm of optoelectronic applications, the optical band gap of materials is indispensable. Diffuse reflectance spectra (DRS) obtained through UV-Vis spectroscopy were employed to calculate the band gap for the prepared nanophosphors. This spectroscopic method assesses the incident light decline following matrix surface absorption or reflection. When referring to powder samples, dispersion occurs more often and it is harder to assess the scattered intensity. Then, for this kind of measurement, the reflection mode is appropriate. Fig. 14(a) exhibits the DRS of LSA and LSA: 4 mol% Er^{3+} in 200–800 nm spectral regions. For the doped optimized sample, different absorption peaks were obtained at 254 nm, 377 nm, 448 nm, 488 nm, and 521 nm due to the charge transfer between oxygen and erbium ion, $^4I_{15/2} \rightarrow {}^4G_{11/2}$, $^4I_{15/2} \rightarrow {}^4F_{5/2}$, $^4I_{15/2} \rightarrow {}^4F_{7/2}$ and $^4I_{15/2} \rightarrow {}^2H_{11/2}$ transitions, respectively. The optical band gap (E_g) is computed using the Kubelka Munk formula provided by[57]

$$F(R) = \frac{K}{S} = \frac{(1-R)^2}{2R} \tag{15}$$

In this relationship, R and $F(R)$ represent diffuse reflectance and Kubelka–Munk absorption function, respectively. The scattering and absorption coefficients are also defined separately by S and K. Tauc's relation is associated with the optical energy gap (E_g) and linear absorption coefficient, which is given below.

$$\alpha h\nu = A[h\nu - E_g]^n \tag{16}$$

In this, A is a constant, $h\nu$ represents the photon's energy, and n stands for the type of transition. Depending on the direct transition, indirect transition, forbidden direct, and forbidden indirect transitions, the value of n may be 1/2, 2, 3, and 3/2, respectively. Eqn (15) and (16) may be used to write the following expression[58]

$$[F(R)h\nu]^2 = C(h\nu - E_g)^n \tag{17}$$

The plot of $[F(R)h\nu]^2$ *vs.* $h\nu$ spectra displayed in Fig. 14(b) indicates the E_g values for the host (E_g = 5.97 eV) and optimized (E_g = 5.51 eV) sample, respectively. The energy gap value reduces on Er^{3+} ion incorporation in the host material.

Table 4 Decay time and quantum efficiency of $La_{1-x}Sr_2AlO_5$:xEr^{3+} (x = 1–7 mol%) phosphors

Sample	τ_{avg} (ms)	A_{nR} (S^{-1})	(η%)
LSA:1 mol% Er^{3+}	1.431	104.01	85.06
LSA:2 mol% Er^{3+}	1.344	149.24	79.95
LSA:3 mol% Er^{3+}	1.227	220.19	72.99
LSA:4 mol% Er^{3+}	1.134	287.03	67.40
LSA:5 mol% Er^{3+}	1.059	349.48	62.99
LSA:6 mol% Er^{3+}	0.978	427.69	58.17
LSA:7 mol% Er^{3+}	0.703	827.64	41.82

3.7 Thermal stability

To assess the luminous features of phosphors for practical use in light-emitting devices, the temperature stability of luminescence is an essential parameter. The temperature-dependent emission spectra of tetragonal $La_{0.96}Sr_2AlO_5$:4 mol% Er^{3+}

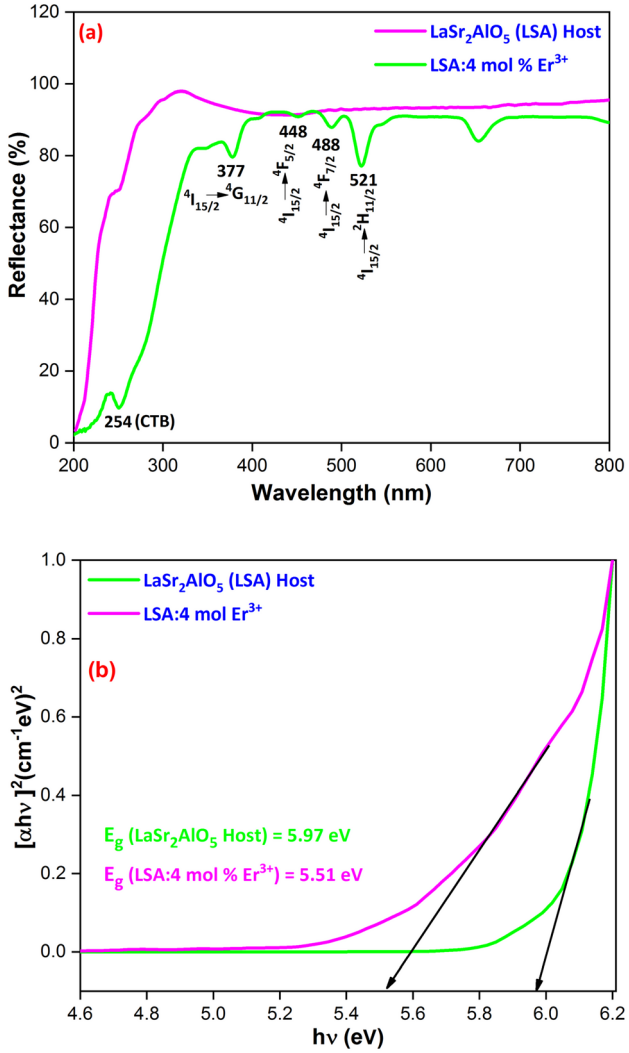

Fig. 14 (a) Diffusion reflectance spectra and the (b) optical band gap of the host and optimized samples.

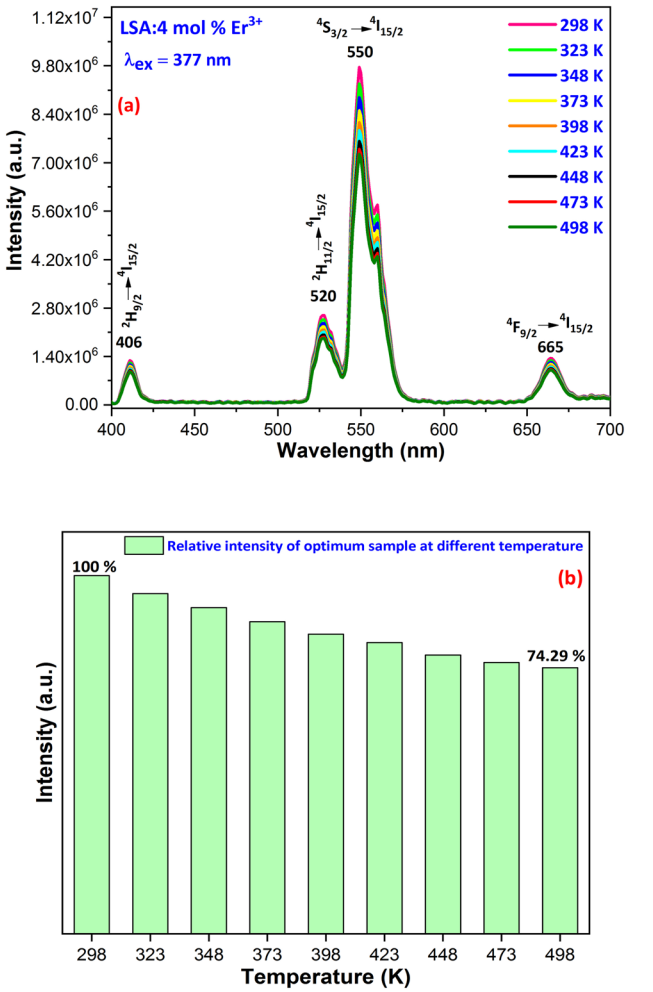

Fig. 15 (a) Temperature-dependent photoluminescence of the $La_{0.96}Sr_2AlO_5$:4 mol% Er^{3+} phosphor; (b) bar intensity graph showing the efficiency as a function of temperature.

phosphors from 298 to 498 K are depicted in Fig. 15(a). Spectral variations become nearly nonexistent as the temperature rises, but the thermal quenching from the nonradiative transition causes their PL intensities to go downward. Additionally, it can be noted that the emission intensity maintains 74.29% of its initial intensity up to 498 K as that of the starting temperature, as displayed in Fig. 15(b), demonstrating the outstanding thermal durability of the developed phosphor. The Arrhenius eqn (18) may be used to describe the thermal activation process that causes the PL emission intensity to drop as the temperature increases.[59]

$$\ln\left(\frac{I_0}{I_T}-1\right)=\ln A-\frac{E_a}{kT} \quad (18)$$

Here, E_a, k, I_T and I_0 are the activation energy, Boltzmann constant, intensity at temperature T, and original intensity, respectively. The relationship of $1/kT$ *vs.* $\ln(I_0/I_T)$ is shown in Fig. 16. The defined data is linearly fitted with a slope of −0.1453, corresponding to E_a = 0.1453 eV. In general, a phosphor with a higher E_a value would be less likely to undergo the non-radiative transition. Consequently, the produced phosphor has a high activation energy value, indicating that it is more resistant to thermal quenching.

3.8 Photometric investigation

Photometric characterization is another method to confirm the color and quality of light generated by the synthesized phosphor material. It covers a wide range of factors, including CIE coordinates, correlated color temperature, and color purity. Eqn (S5)† was employed to analyze chromaticity points (x, y) in accordance with CIE-1931.[60] The tristimulus values for the fundamental red, green, and blue colors are shown as X, Y, and Z, correspondingly. The CIE chromaticity diagram for the phosphor under investigation is shown in Fig. S1–S7.† The ratio of the spacing between the pure white coordinates (x_i, y_i) and computed CIE coordinates (x, y) to the separation dominant wavelength (x_d, y_d) and pure white coordinates (x_i, y_i) is known as color purity.[61]

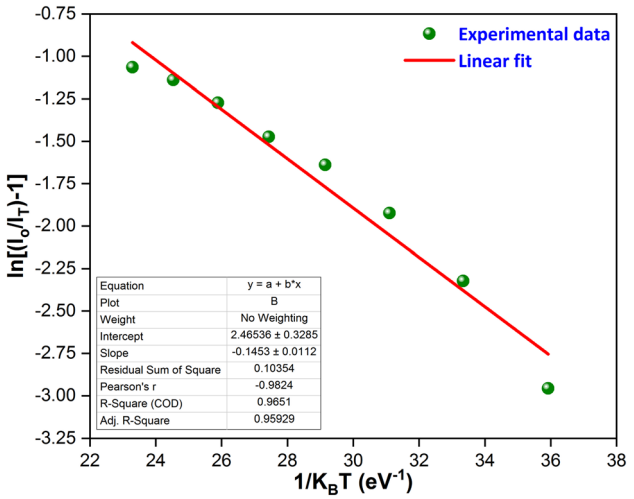

Fig. 16 Linear fitted graph between $\ln[(I_0/I_T) - 1]$ *vs.* $1/KT$ for the $La_{0.96}Sr_2AlO_5$:4 mol% Er^{3+} phosphor.

Table 5 Chromaticity parameters of $La_{1-x}Sr_2AlO_5:xEr^{3+}$ (x = 1–7 mol%) nanophosphors

Sample	(x, y)	CP (%)	(u', v')	CCT (K)
LSA:1 mol% Er^{3+}	0.3129, 0.6636	94.6	0.1211, 0.5777	4238
LSA:2 mol% Er^{3+}	0.3135, 0.6601	93.6	0.1218, 0.5771	4632
LSA:3 mol% Er^{3+}	0.3132, 0.6491	89.5	0.1233, 0.5748	4388
LSA:4 mol% Er^{3+}	0.3139, 0.6364	92.4	0.1255, 0.5722	4127
LSA:5 mol% Er^{3+}	0.3132, 0.6491	90.1	0.1233, 0.5748	4237
LSA:6 mol% Er^{3+}	0.3101, 0.6564	91.2	0.1209, 0.5760	4362
LSA:7 mol% Er^{3+}	0.3124, 0.6510	90.4	0.1227, 0.5751	4491

$$CP = \sqrt{\frac{(x - x_i)^2 + (y - y_i)^2}{(x_d - x_i)^2 + (y_d - y_i)^2}} \times 100 \quad (19)$$

The temperature at which a phosphor emits the same color as an ideal blackbody is known as its CCT value. The McCamy relation (20) is mathematically used to get the CCT values of each produced phosphor.[62]

$$CCT = -437n^3 + 3601n^2 - 6861n + 5514.31 \quad (20)$$

Here, n is $(x - x_e)/(y - y_e)$ is the inverse slope line with x_e and y_e known as convergence epicenters having values of 0.332 and 0.186, respectively. The computation includes changing the CIE point (x, y to u', v') to evaluate the color temperature data using eqn (S6).† Fig. S8–S14† display the CIE 1976 color profile of Er^{3+} (1–7 mol%) doped LSA nanophosphors associated with their CCT values. In general, cold light suitable for commercial usage corresponds to CCT values of more than 3000 K. On the other hand, warm light has a CCT value of less than 3000 K and is a potential candidate for indoor lighting in the SSL area. The computed values of (x, y), color purity, CCT, and (u', v') are summarized in Table 5.

4 Conclusions

This article demonstrates the simple and faster gel-combustion approach that is employed to produce $LaSr_2AlO_5:Er^{3+}$ phosphors. The XRD method was utilized to investigate the phase purity and structure of the synthesized materials. The XRD peaks indicate increased phase purity and higher crystallinity, which improves the optical characteristics of phosphor materials. Rietveld refinement of the XRD data provides an accurate depiction of the crystal structure, including the dimension of the unit cell, atomic position coordinates, and the structure generated by every atom with neighboring atoms. The produced samples are in space group $I4/mcm$ of the tetragonal crystal structure. TEM images display almost spherical particles, agglomerated with uneven-sized particles in the synthesized material. EDX profiles show the presence of all atoms and define the composition of the prepared materials. Following Er^{3+} doping, the energy band gap has been observed to reduce, demonstrating the Burstein–Moss effect. On 377 nm UV excitation, the phenomena of down conversion photoluminescence were investigated in detail. At 550 nm, the strongest peak was observed, producing a vivid green color corresponding to the $^4I_{15/2} \rightarrow {}^4G_{11/2}$ transition of Er^{3+} ions. Concentration quenching resulted in a decline in PL intensity beyond 4 mol% when the doping concentration of Er^{3+} was increased. Multipolar (quadrupole–quadrupole) interaction was the predominant interaction during concentration quenching. Thermal quenching is shown to have an activation energy of 0.1453 eV. All of the aforementioned findings imply that the suggested $LaSr_2AlO_5:Er^{3+}$ phosphor, which emits green light and has exceptional luminescent properties, would be a potential material for solid-state lighting.

Data availability

Data will be made available on request.

Author contributions

Pawan Kumar: data curation, writing – original draft, investigation, methodology; Devender Singh: writing – review & editing, resources, supervision; Harish Kumar: software.

Conflicts of interest

The authors declare that they have no known competing financial interests or personal relationships that could have appeared to influence the work reported in this paper.

Acknowledgements

Pawan Kumar is thankful to UGC-New Delhi for providing SRF [117/(CSIRNETJUNE2019)]. Devender Singh is grateful to MDU, Rohtak, for a Post Seed Grant under the research promotion scheme.

References

1 E. Pavitra, G. S. R. Raju, S. M. Ghoreishian, C. H. Kwak, J. Y. Park, Y. K. Han and Y. S. Huh, Novel orange-emitting Ba_2LaNbO_6:Eu^{3+} nanophosphors for NUV-based WLEDs and photocatalytic water purification, *Ceram. Int.*, 2019, **45**, 4781–4789.

2 B. Marí, K. C. Singh, P. Cembrero-Coca, I. Singh, D. Singh and S. Chand, Red emitting $MTiO_3$ (M = Ca or Sr) phosphors doped with Eu^{3+} or Pr^{3+} with some cations as co-dopants, *Displays*, 2013, **34**, 346–351.

3 K. Nehra, A. Dalal, A. Hooda, D. Singh and S. Kumar, Exploration of newly synthesized red luminescent material of samarium for display applications, *Inorg. Chem. Commun*, 2022, **139**, 109361.

4 K. Nehra, A. Dalal, A. Hooda, K. Jakhar, D. Singh and S. Kumar, Preparation, optoelectronic and spectroscopic analysis of fluorinated heteroleptic samarium complexes for display applications, *Inorg. Chim. Acta*, 2022, **537**, 120958.

5 X. Huang, Q. Sun and B. Devakumar, Facile low-temperature solid-state synthesis of efficient blue-emitting $Cs_3Cu_2I_5$ powder phosphors for solid-state lighting, *Mater. Today Chem.*, 2020, **17**, 100288.

6 P. Kumar, D. Singh, I. Gupta, S. Singh, S. Nehra and R. Kumar, A study of phase evolution, crystallographic and down-conversion luminescent behaviour of monoclinic $Y_4Al_2O_9$:Dy^{3+} nanophosphors for white light applications, *Opt. Mater.*, 2023, **138**, 113677.

7 I. Gupta, S. Singh, S. Bhagwan and D. Singh, Rare earth (RE) doped phosphors and their emerging applications: a review, *Ceram. Int.*, 2021, **47**, 19282–19303.

8 I. Gupta, P. Kumar, S. Singh, S. Bhagwan, V. Kumar and D. Singh, Phase recognition, structural measurements and photoluminescence studies of reddish-orange-emissive $YAlO_3$:Sm^{3+} perovskite nanophosphors for NUV energized WLEDs, *J. Mol. Struct.*, 2022, **1267**, 133567.

9 D. Singh, S. Bhagwan, A. Dalal, K. Nehra, K. Singh, A. Simantilleke and I. Singh, Intense red luminescent materials of ternary Eu^{3+} complexes of oxide ligands for electroluminescent display devices, *Optik*, 2020, **208**, 164111.

10 C. M. Nandanwar, N. S. Kokode, A. N. Yerpude and S. J. Dhoble, Synthesis and photoluminescence study of $KCaPO_4$:Eu^{3+} phosphors for solid state lighting, *Mater. Lett.: X*, 2023, **18**, 100202.

11 P. Kumar, D. Singh, I. Gupta, S. Singh, S. Nehra and R. Kumar, Combustion derived single phase $Y_4Al_2O_9$:Tb^{3+} nanophosphor: crystal chemistry and optical analysis for solid state lighting applications, *RSC Adv.*, 2023, **13**, 7752–7765.

12 D. Singh, V. Tanwar, A. P. Simantilleke, S. Bhagwan, B. Mari, P. S. Kadyan and I. Singh, Synthesis and enhanced luminescent characterization of $SrAl_4O_7$:Eu^{2+}, RE^{3+} (RE = Nd, Dy) nanophosphors for light emitting applications, *J. Mater. Sci.: Mater. Electron.*, 2016, **27**, 5303–5308.

13 C. Li, X. M. Wang, Z. P. Yang and H. Jiao, $Ca_8Mg_7Si_9N_{22}$:Ce^{3+}—a yellow-emitting nitride phosphor for white light emitting diodes, *ACS Appl. Electron. Mater.*, 2020, **2**, 936–943.

14 P. Kumar, D. Singh, I. Gupta and H. Kumar, Influence of Dy^{3+} ion concentration on structural, photoluminescence and energy transfer mechanism of promising $GdSr_2AlO_5$ nanophosphors for white light applications, *Ceram. Int.*, 2023, **49**, 29010–29024.

15 S. D. Han, I. Singh, D. Singh, Y. H. Lee and G. Sharma, Crystal growth of electroluminescent ZnS:Cu, Cl phosphor and its TiO_2 coating by sol–gel method for thick-film EL device, *J. Lumin.*, 2005, **115**, 97–103.

16 P. Kumar, D. Singh, I. Gupta, S. Singh, S. Nehra and R. Kumar, Er^{3+}-doped $Y_4Al_2O_9$ nanophosphors for advance display applications: synthesis, crystal chemistry and down conversion photoluminescent investigation, *Mater. Chem. Phys.*, 2023, **301**, 127610.

17 A. Dalal, K. Nehra, A. Hooda, S. Singh, S. Bhagwan, D. Singh and S. Kumar, 2, 2′-Bipyridine based fluorinated β-Diketonate Eu(III) complexes as red emitter for display applications, *Inorg. Chem. Commun.*, 2022, **140**, 109399.

18 D. Singh, S. Sheoran, V. Tanwar and S. Bhagwan, Optical characteristics of Eu(III) doped $MSiO_3$ (M = Mg, Ca, Sr and Ba) nanomaterials for white light emitting applications, *J. Mater. Sci.: Mater. Electron.*, 2017, **28**, 3243–3253.

19 D. Singh, V. Tanwar, A. P. Samantilleke, B. Mari, S. Bhagwan, P. S. Kadyan and I. Singh, Preparation and Photoluminescence Properties of $SrAl_2O_4$:Eu^{2+}, RE^{3+} Green Nanophosphors for Display Device Applications, *J. Electron. Mater.*, 2016, **45**, 2718–2724.

20 L. Zhang, Y. Xie, X. Geng, B. Deng, H. Geng and R. Yu, Double perovskite Ca_2MgTeO_6:Eu^{3+} red-emitting phosphors with high thermal stability for near UV/blue excited white LEDs, *J. Lumin.*, 2020, **225**, 117365.

21 P. Kumar, S. Singh, I. Gupta, V. Kumar and D. Singh, Preparation and luminescence behaviour of perovskite $LaAlO_3$:Tb^{3+} nanophosphors for innovative displays, *Optik*, 2022, **267**, 169709.

22 P. Kumar, D. Singh, I. Gupta, S. Singh, V. Kumar, H. Kumar and S. K. Chhikara, Cool green light emitting $GdAlO_3$:Tb^{3+} perovskite nanomaterials: crystal structure and spectroscopic characteristics for advance display appliances, *Inorg. Chem. Commun.*, 2022, **145**, 110064.

23 Z. Yu, Z. Xia, C. Su, R. Wang and Q. Liu, Effect of Gd/La substitution on the phase structures and luminescence properties of (La, Gd) Sr_2AlO_5:Ce^{3+} solid solution phosphors, *J. Mater. Chem. C*, 2015, **3**, 11629–11634.

24 J. H. Kim and K. Y. Jung, Preparation and luminescence characterization of fine-sized $LaSr_2AlO_5$:Ce phosphor prepared by spray pyrolysis, *J. Lumin.*, 2011, **131**, 1487–1491.

25 I. Gupta, D. Singh, P. Kumar, S. Singh, S. Bhagwan and V. Kumar, Crystallographic and luminescence studies of $Gd_2Si_2O_7$:Er^{3+} nanomaterials for NUV energized lighting applications, *J. Mol. Struct.*, 2023, **1287**, 135595.

26 S. Singh, V. Tanwar, A. P. Simantilleke and D. Singh, Structural and photoluminescent investigations of $SrAl_2O_4$:Eu^{2+}, RE^{3+} improved nanophosphors for solar cells, *Nano-Struct. Nano-Objects*, 2020, **21**, 100427.

27 S. Singh and D. Singh, Structural and optical properties of green emitting Y_2SiO_5:Tb^{3+} and Gd_2SiO_5:Tb^{3+} nanoparticles for modern lighting applications, *Rare Met.*, 2021, **40**, 3289–3298.

28 I. Gupta, P. Kumar, S. Singh, S. Bhagwan, S. K. Chhikara and D. Singh, Crystal configuration, spectroscopic and optical characteristics of Er^{3+} doped $YAlO_3$ perovskites for advanced photonic appliances, *Inorg. Chim. Acta*, 2022, **543**, 121183.

29 M. He, K. Liu, B. Dong, J. Cai, H. Zhao and Z. Zhang, Luminescent properties and mechanism study of Yb^{3+}/Er^{3+} Co-doped $GdBa_3B_9O_{18}$ phosphors, *Opt. Mater.*, 2022, **127**, 112300.

30 S. Vignesh, S. Suganthi, J. K. Sundar, V. Raj and P. R. I. Devi, Highly efficient visible light photocatalytic and antibacterial performance of PVP capped Cd:Ag:ZnO photocatalyst nanocomposites, *Appl. Surf. Sci.*, 2019, **479**, 914–929.

31 L. Gomez De Arco, Y. Zhang, C. W. Schlenker, K. Ryu, M. E. Thompson and C. Zhou, Continuous, highly flexible, and transparent graphene films by chemical vapor deposition for organic photovoltaics, *ACS Nano*, 2010, **4**, 2865–2873.

32 P. Kumar, S. Singh, I. Gupta, V. Kumar and D. Singh, Structural and optical characterization of trivalent samarium-activated $LaAlO_3$ nanocrystalline materials for solid-state lighting, *J. Mol. Struct.*, 2022, **1265**, 133362.

33 V. Tanwar, S. Singh, I. Gupta, P. Kumar, H. Kumar, B. Mari and D. Singh, Preparation and luminescence characterization of Eu(III)-activated Forsterite for optoelectronic applications, *J. Mol. Struct.*, 2022, **1250**, 131802.

34 P. Kumar, S. Singh, I. Gupta, V. Kumar and D. Singh, Luminous $LaAlO_3$:Dy^{3+} perovskite nanomaterials: synthesis, structural, and luminescence characteristics for white light-emitting diodes, *Luminescence*, 2022, **37**, 1932–1941.

35 P. Kumar, S. Singh, I. Gupta, K. Nehra, V. Kumar and D. Singh, Structural and luminescent behaviour of Dy(III) activated $Gd_3Al_5O_{12}$ nanophosphors for white-LEDs applications, *Mater. Chem. Phys.*, 2023, **295**, 127035.

36 P. Kumar, S. Singh, I. Gupta, K. Nehra, V. Kumar and D. Singh, Structural refinement and optical characteristics of single-phase $Gd_3Al_5O_{12}$:Er^{3+} nanophosphors for luminescent applications, *J. Lumin.*, 2022, **252**, 119338.

37 I. Gupta, D. Singh, S. Singh, P. Kumar, S. Bhagwan and V. Kumar, Study of structural and spectroscopic characteristics of novel color tunable yellowish-white Dy^{3+} doped $Gd_4Al_2O_9$ nanophosphors for NUV-based WLEDs, *J. Mol. Struct.*, 2023, **1272**, 134199.

38 I. Gupta, D. Singh, S. Singh, P. Kumar, S. Bhagwan and V. Kumar, Phase recognition and spectroscopic characteristics of single-phase Tb^{3+} doped $Gd_4Al_2O_9$ nanophosphors for NUV energized advanced photonic appliances, *J. Lumin.*, 2022, **252**, 119327.

39 G. U. Xiguang, F. U. Renli, W. Jiang, P. Zhang, T. A. N. G. Ye and A. CoŞGun, Photoluminescence properties of an orange-red $LaSr_2AlO_5$:Sm^{3+} phosphor prepared by the Pechini-type sol-gel process, *J. Rare Earths*, 2015, **33**, 954–960.

40 P. Kumar, S. Singh, I. Gupta, A. Hooda, V. Kumar and D. Singh, Reddish-orange color tunable Sm^{3+} activated $Gd_3Al_5O_{12}$ phosphors: crystallographic and photophysical investigation for lighting applications, *J. Mol. Struct.*, 2023, **1271**, 134074.

41 P. Kumar, S. Singh, I. Gupta, A. Dalal, V. Kumar and D. Singh, Preparation, structural and photometric properties of single-phased $Gd_3Al_5O_{12}$:Tb^{3+} green-emitting phosphors for solid state lighting purpose, *Mater. Sci. Eng., B*, 2023, **288**, 116189.

42 P. Kumar, D. Singh, I. Gupta, S. Singh, S. Nehra and R. Kumar, Realization of warm reddish-orange light emitter single phase $Y_4Al_2O_9$:Sm^{3+} nanophosphors for indoor lighting applications, *J. Lumin.*, 2023, **257**, 119703.

43 K. A. Aly, N. M. Khalil, Y. Algamal and Q. M. Saleem, Lattice strain estimation for $CoAl_2O_4$ nano particles using Williamson-Hall analysis, *J. Alloys Compd.*, 2016, **676**, 606–612.

44 N. Khlifi, N. Ihzaz, S. Mrabet, A. Alyamani and L. El Mir, X-ray peaks profile analysis, optical and cathodoluminescence investigations of cobalt-doped ZnO nanoparticles, *J. Lumin.*, 2022, **245**, 118770.

45 P. Kumar, D. Singh, I. Gupta, S. Singh, V. Kumar, H. Kumar and S. K. Chhikara, Cool green light emitting $GdAlO_3$:Dy^{3+} perovskite nanomaterials: crystal structure and spectroscopic characteristics for advance display appliances, *Inorg. Chem. Commun.*, 2022, **154**, 110064.

46 S. Wang, B. Devakumar, Q. Sun, J. Liang, L. Sun and X. Huang, Highly efficient near-UV-excitable $Ca_2YHf_2Al_3O_{12}$:Ce^{3+}, Tb^{3+} green-emitting garnet phosphors with potential application in high color rendering warm-white LEDs, *J. Mater. Chem. C*, 2020, **8**, 4408–4420.

47 W. B. Im, N. N. Fellows, S. P. DenBaars, R. Seshadri and Y. I. Kim, $LaSr_2AlO_5$, a versatile host compound for Ce^{3+}-based yellow phosphors: structural tuning of optical properties and use in solid-state white lighting, *Chem. Mater.*, 2009, **21**, 2957–2966.

48 I. Gupta, D. Singh, S. Singh, P. Kumar, S. Bhagwan and V. Kumar, Structural and luminescent features of warm reddish-orange light-emitting Sm(III) doped $Gd_2Si_2O_7$ nanophosphors for near UV-energized LEDs, *J. Lumin.*, 2023, **263**, 120007.

49 P. Kumar, D. Singh, I. Gupta, S. Singh and V. Kumar, Structural and luminescent characteristics of orthorhombic $GdAlO_3$:Sm^{3+} nanocrystalline materials for solid state lighting, *Chem. Phys. Lett.*, 2022, **812**, 140277.

50 P. Kumar, S. Singh, I. Gupta, V. Kumar and D. Singh, Er^{3+} activated $LaAlO_3$ perovskite phosphor: crystal structure and down conversion photoluminescent behaviour for optoelectronic devices, *Inorg. Chem. Commun.*, 2022, **141**, 109578.

51 P. Kumar, D. Singh, I. Gupta and H. Kumar, Synthesis, crystallographic structure, down shifting luminescence of Er(III) activated $GdSr_2AlO_5$ nanophosphors: an efficient

green emitter for solid state lighting, *Mater. Sci. Semicond. Process.*, 2023, **167**, 107765.

52 P. Kumar, D. Singh, I. Gupta, S. Singh and V. Kumar, Emerging green light emission of Er^{3+}-activated single phased $GdAlO_3$ phosphors for lighting applications, *Luminescence*, 2022, **37**, 2028–2040.

53 R. T. Maske, A. N. Yerpude, R. S. Wandhare, A. Nande and S. J. Dhoble, Combustion synthesized novel $SrAlBO_4:Eu^{3+}$ phosphor: structural, luminescence, and Judd-Ofelt analysis, *Opt. Mater.*, 2023, **141**, 113893.

54 M. Guzik, E. Tomaszewicz, Y. Guyot, J. Legendziewicz and G. Boulon, Spectroscopic properties, concentration quenching and Yb^{3+} site occupations in vacancied scheelite-type molybdates, *J. Lumin.*, 2016, **169**, 755–764.

55 I. Gupta, S. Singh, P. Kumar, S. Bhagwan, V. Tanwar, S. Nehra, V. Kumar and D. Singh, Synthetic, structural and optical characteristic of novel color tunable reddish-orange $Gd_4Al_2O_9:Sm^{3+}$ nanocrystalline materials for solid-state photonic appliances, *Inorg. Chem. Commun.*, 2023, **148**, 110332.

56 I. Gupta, S. Singh, P. Kumar, S. Bhagwan, V. Kumar and D. Singh, Structural, morphological and optoelectronic aspects of $YAlO_3:Dy^{3+}$ doped nanocrystalline materials for NUV energized WLEDs, *Curr. Appl. Phys.*, 2022, **43**, 78–89.

57 Y. Wang, Z. Liang, K. Jiang, Y. Lin, D. He, J. Liu and R. Yu, $SrLaNaTeO_6:Eu^{3+}$ red-emitting phosphors with high luminescence efficiency and high thermal stability for high CRI white LEDs, *Ceram. Int.*, 2023, **49**, 579–590.

58 K. Shwetabh, M. M. Upadhyay and K. Kumar, Synthesis and upconversion emission studies of $CaYF_5:Ho^{3+}/Yb^{3+}$ phosphor and its applications in optical thermometry, fingerprint detection, and security ink, *RSC Adv.*, 2023, **13**, 9377–9386.

59 S. Bi, H. Cheng, M. Luo, P. Cai and L. Qin, Synthesis, crystal structure and luminescent properties of Eu^{3+}-activated halotungstates applied in W-LEDs, *Ceram. Int.*, 2023, **49**, 18592–18601.

60 J. Xie, L. Cheng, H. Tang, X. Yu, Z. Wang, X. Mi, Q. Liu and X. Zhang, A new single-phase $NaBi(WO_4)_2:Dy^{3+}$, Eu^{3+} phosphor with excellent thermal stability for NUV-excited warm white LEDs, *J. Alloys Compd.*, 2021, **882**, 160589.

61 P. Kumar, D. Singh and I. Gupta, UV excitable $GdSr_2AlO_5:Eu^{3+}$ red emitting nanophosphors: structure refinement, photoluminescence, Judd-Ofelt analysis and MTithermal stability for w-LEDs, *J. Alloys Compd.*, 2023, **966**, 171410.

62 K. Nehra, A. Dalal, A. Hooda, P. Kumar, D. Singh, S. Kumar and P. Kumar, Luminous terbium and samarium complexes with diacetylmethane and substituted 1,10-phenanthroline derivatives for display applications: preparation and optoelectronic, *J. Lumin.*, 2022, **249**, 119032.